

Destruction of Long-Period Comets

David Jewitt¹

¹Department of Earth, Planetary and Space Sciences, UCLA,
595 Charles Young Drive East, Los Angeles, CA 90095-1567, USA

jewitt@ucla.edu

Received _____; accepted _____

The Astronomical Journal

ABSTRACT

We identify a sample of 27 long-period comets for which both non-gravitational accelerations and Lyman- α based gas production rates are available. Seven of the 27 comets (i.e. $\sim 25\%$) did not survive perihelion because of nucleus fragmentation or complete disintegration. Empirically, the latter nuclei have the smallest gas production rates and the largest non-gravitational accelerations, which are both indicators of small size. Specifically, the disintegrating nuclei have a median radius of only 0.41 km, one quarter of the 1.60 km median radius of those surviving perihelion. The disintegrating comets also have a smaller median perihelion distance (0.48 au) than do the survivors (0.99 au). We compare the order of magnitude timescale for outgassing torques to change the nucleus spin, τ_s , with the time spent by each comet in strong sublimation, Δt , finding that the disrupted comets are those with $\tau_s < \Delta t$. The destruction of near-Sun long-period comets is thus naturally explained as a consequence of rotational break-up. We discuss this process as a contributor to Oort’s long mysterious “fading parameter”.

Subject headings: comets: general—comets:

1. INTRODUCTION

Comets are volatile-rich products of accretion in the Sun’s protoplanetary disk. Historically, comets were classified as either short-period or long-period, depending on whether their orbital periods were less or greater than 200 years. With some complications and subtleties, this division into two dynamical groups has survived to the present day. Most short-period (strictly “Jupiter family”) comets arrive from the Kuiper belt, where they have been stored for the last 4.5 Gyr at temperatures ~ 40 K. Long-period comets arrive from equally long-term residence in the Oort cloud, where the equilibrium temperature is $\lesssim 10$ K. Both short and long-period comets are thought to have formed in the giant planet region of the solar system and were scattered to their respective storage reservoirs in the final stages of the growth of the planets.

Oort (1950) first examined the distribution of orbital binding energies of long-period comets and found that no purely dynamical model could fit the large observed ratio of first-appearance (“dynamically new”) comets to returning comets. He invoked an ad-hoc “fading parameter” by which to decrease the brightness of returning comets and thereby to depress their number in magnitude limited surveys. Subsequent work with a much larger comet sample verified both the dynamics and the need for a fading parameter (Wiegert & Tremaine 1999; Levison et al. 2002) but did not identify its physical origin. Observationally, Bortle (1991) reported that intrinsically faint long-period comets with small perihelia are less likely to survive perihelion than their brighter counterparts but, again, did not identify the mechanism.

Several practical difficulties are inherent in the observational study of long-period comets. Crucially, these objects are generally discovered only a short time before perihelion and they are soon thereafter lost as they recede from the Sun and fade to permanent invisibility. The observational window for long-period comets is consequently short, unlike

that of the short-period comets, which can be predictably observed over many orbits. Even worse, long-period comets with perihelia < 1 au must be observed at small solar elongation (Sun-Earth-comet) angles, where ground-based telescopes struggle against low elevation and high sky-brightness constraints. As a result of these practical difficulties, the nuclei of long-period comets are poorly characterized relative to those of short-period comets. Cometary disintegrations, being intrinsically unpredictable and rapidly evolving, are even more difficult to study and rarely reach publication in the refereed literature.

2. THE COMET SAMPLE

We are interested in long-period comets for which there exist both reliable measurements of the total outgassing rates and of the non-gravitational accelerations. For this reason, we focus on long-period comets discovered since the year 2000, to coincide with the period in which high quality physical and dynamical measurements have become routinely available from long-term surveys. Specifically, we rely on systematic measurements of the water production rate obtained from Lyman- α observations with the space-borne SWAN ultraviolet spectrometer aboard SOHO (Bertaux et al. 1997), and on all-sky optical surveys (e.g. the Catalina and, recently, Pan STARRS surveys) which provide precise astrometry over a long timebase. We further restricted the sample to comets with perihelion distances $q \leq 2$ au.

2.1. Non-gravitational Accelerations:

We used orbit solutions from JPL’s Horizons¹ web site to compile a list of LPCs showing evidence for non-gravitational acceleration. The orbital properties of the 27 comets used for this study are listed in Table 1, where we show the estimated original barycentric orbital elements in order to avoid the effects of planetary perturbations. (To find the latter, we used Horizons to compute the osculating orbital elements on 1900-Jan-01, a time at which all of the comets in the present study were far beyond the planetary region and therefore subject to minimal planetary perturbation). Twelve of the 27 comets are retrograde (inclination $i \geq 90^\circ$), consistent with being drawn from an isotropic distribution, and the eccentricities are all very close to $e = 1$. By default, non-gravitational parameters are computed when purely gravitational orbits fail to reproduce astrometric data, but otherwise are assumed to be zero. Conventionally, the non-gravitational acceleration is resolved into three, orthogonal components (A_1 , A_2 and A_3 , expressed in au day^{-2}), with A_1 being in the radial direction, A_3 perpendicular to the plane of the orbit and A_2 perpendicular to A_1 and A_3 (Marsden et al. 1973). The radial component, A_1 , is normally dominant, because cometary mass loss is concentrated on the heated, sun-facing side of the nucleus producing a recoil force that acts away from the Sun. Gas produced by the sublimation of cometary water ice dominates the instantaneous outflow momentum from the nucleus. For this reason, it is conventional to scale the acceleration by a function representing the instantaneous equilibrium sublimation rate, expressed as $g(r_H)$, such that the total acceleration is

$$\alpha_{NG} = g(r_H) (A_1^2 + A_2^2 + A_3^2)^{1/2}. \quad (1)$$

Function $g(r_H)$ is defined by

¹<http://ssd.jpl.nasa.gov/horizons.cgi>

$$g(r_H) = \alpha_M \left(\frac{r_H}{r_0}\right)^{-m} \left[1 + \left(\frac{r_H}{r_0}\right)^n\right]^{-k} \quad (2)$$

where $r_0 = 2.808$ au, $m = 2.15$, $n = 5.093$, $k = 4.6142$, and $\alpha_M = 0.1113$ are constants determined from a fit to a model of sublimation and the normalization is such that $g(1) = 1$ (Marsden et al. 1973). These constants derive from a model of a sublimating isothermal sphere. While this is logically incorrect (since an isothermal sphere would sublimate isotropically and hence experience no net recoil force), the difference from a physically more plausible hemispheric sublimator is minor, at least at distances $r_H \lesssim 3$ au where the bulk of the absorbed energy is used to break hydrogen bonds in water and the sublimation rate is large. The assumed nucleus temperature distribution over the nucleus surface matters more at larger distances, but the sublimation rate falls exponentially and the resulting recoil force due to distant activity is comparatively small. Values of A_1 , A_2 and A_3 and α_{NG} are listed for each comet in Table 2. The accelerations are small (the median value at 1 au is $\alpha_{NG} = 4 \times 10^{-7}$ m s⁻², about 0.007% of the solar gravitational acceleration).

2.2. Production Rates:

We searched the literature to find reliable measurements of the mass production rates from those long-period comets having non-zero non-gravitational accelerations. Water molecules dominate the mass flux and outflow momentum from the nucleus. Direct measurements of the water production rate are impractical, but observations of water photodissociation products provide an accurate alternative. We placed the greatest reliance on a long and spectacular series of measurements of Lyman- α emission from cometary hydrogen, a photodissociation product of water, made using the SWAN mapping spectrometer instrument on the SOHO spacecraft (Bertaux et al. 1997). These measurements (Combi et al. 2008, 2009, 2011, 2014, 2018, 2019, 2021, 2021) have the

advantage of internal consistency, being made using a single instrument and, in many cases, providing time resolution sufficient to monitor the heliocentric variation of the water production. Where necessary, we used other published production rate data as listed in Table 2.

Production rates measured as a function of heliocentric distance were interpolated to estimate the production rate at $r_H = 1$ au, denoted $Q_{H_2O}(1)$, and listed in Table 2. Some comets display significant asymmetry, such that $Q_{H_2O}(1)$ differs before and after perihelion. In these cases we list the average value. We estimate that the values of $Q_{H_2O}(1)$ in the table are accurate to no better than a factor of ~ 2 . The mass production rate at 1 au, $\dot{M}(1)$ kg s⁻¹, is related to $Q_{H_2O}(1)$ by $\dot{M}(1) = \mu m_H Q_{H_2O}(1)$, where $\mu = 18$ is the molecular weight of the water molecule, and $m_H = 1.67 \times 10^{-27}$ kg is the mass of the hydrogen atom. For reference, we note that a production rate $Q_{H_2O}(1) = 10^{29}$ s⁻¹ corresponds to $\dot{M} = 3000$ kg s⁻¹. We assume that gas produced on the nucleus surface flows away at the thermal speed $V_{th} = (8kT/(\pi\mu m_H))^{1/2}$, where $k = 1.38 \times 10^{-23}$ J K⁻¹ is the Boltzmann constant and T is the temperature of the sublimating ice surface. At 1 au, the temperature is depressed by sublimation to about $T = 200$ K, giving $V_{th} = 500$ m s⁻¹. The temperature and V_{th} change only slightly with heliocentric distance as a result of buffering by sublimation. We ignore solid matter (“dust”) expelled simultaneously from the comets because, although the dust and gas mass production rates may be comparable, the dust mass is dominated by large particles which are poorly coupled to the gas flow, travel at speeds $\ll V_{th}$, and so carry only a small fraction of the outflow momentum.

3. RESULTS

3.1. Nucleus Radii

We use the production rate and non-gravitational acceleration data to estimate the radii of the nuclei in two ways.

a) Radius from Total Production Rate:

In equilibrium with sunlight, sublimation of cometary ice drives a mass flux, f_s ($\text{kg m}^{-2} \text{ s}^{-1}$), from the surface. Measurements of comets show that sublimation from the nucleus night-side is weak because surface temperatures there are very low. Accordingly, we represent the nucleus as a sphere, sublimating only from the day-side hemisphere, and we use the energy balance equation to calculate f_s ;

$$\frac{L_{\odot}(1 - A_B)}{4\pi r_H^2} = 2 [\epsilon\sigma T^4 + f_s(T)H(T)]. \quad (3)$$

Here, the term on the left is the absorbed solar power ($L_{\odot} = 4 \times 10^{26} \text{ W}$ is the solar luminosity, $A_B = 0.04$ the assumed Bond albedo), the first term on the right accounts for radiation cooling ($\epsilon = 0.9$ is the assumed emissivity, $\sigma = 5.67 \times 10^{-8} \text{ W m}^{-2} \text{ K}^{-4}$ is the Stephan-Boltzmann constant and T is the effective temperature) and the second term represents energy consumed in sublimating ice the latent heat of which is $H = 2 \times 10^6 \text{ J kg}^{-1}$). Equation 3 is solved using the Clausius-Clapeyron equation for the pressure vs. temperature along the sublimation phase change boundary. At $r_H = 1 \text{ au}$, for sublimation averaged over the dayside of a spherical ice nucleus, we find $f_s = 2.1 \times 10^{-4} \text{ kg m}^{-2} \text{ s}^{-1}$.

The mass loss rate, \dot{M} (kg s^{-1}), is then

$$\dot{M} = 2\pi r_n^2 f_A f_s \quad (4)$$

where r_n is the nucleus radius. The factor f_A represents the fraction of the surface area of the nucleus that contributes to the sublimation flux. Empirically, f_A is a decreasing function of nucleus radius and approaches unity on sub-kilometer short-period comets (Jewitt 2021a). (This trend is probably a result of observational bias favoring the detection of small cometary nuclei having large active fractions over those with less active surfaces). Values $f_A > 1$ are possible if ice sublimates both from the nucleus and from icy grains ejected from the nucleus. From Equation 4 we obtain the nucleus radius

$$r_1 = \left(\frac{\dot{M}}{2\pi f_A f_s} \right)^{1/2} \quad (5)$$

and the nucleus mass

$$M_n(1) = \rho_n \left(\frac{2}{9\pi} \right)^{1/2} \left(\frac{\dot{M}}{f_A f_s} \right)^{3/2}. \quad (6)$$

As a starting point, and in the absence of evidence regarding f_A on the long-period nuclei, we take $f_A = 1$. Values of r_1 are listed for each comet in Table 3. If $f_A < 1$, as in most short-period comets (A’Hearn et al. 1995), then r_1 gives an under-estimate of the true radius.

b) Radius from Non-Gravitational Acceleration: Non-gravitational acceleration, α_{NG} , is the result of anisotropic mass loss from sublimating ices on the nucleus. We use it to obtain a second estimate of the mass of the nucleus.

The force on the nucleus is $k_R \dot{M} V_{th}$, where V_{th} is the outflow speed and $0 \leq k_R \leq 1$ is a dimensionless constant expressing the fraction of the outflow momentum that goes into

accelerating the nucleus (for isotropic outgassing, $k_R = 0$, while for perfectly collimated outgassing $k_R = 1$). Then, force balance on a spherical nucleus of density ρ_n gives a second relation for the nucleus radius

$$r_2 = \left(\frac{3k_R \dot{M} V_{th}}{4\pi \rho_n \alpha_{NG}} \right)^{1/3} \quad (7)$$

and the nucleus mass is

$$M_n(2) = \frac{k_R \dot{M} V_{th}}{\alpha_{ng}}. \quad (8)$$

We take the measured values of \dot{M} and α_{NG} from Table 2 and, as noted above, we adopt $\rho_n = 500 \text{ kg m}^{-3}$ and $V_{th} = 500 \text{ m s}^{-1}$. Measurements from 67P/Churyumov-Gerasimenko give $k_R = 0.5$ (Jewitt et al. (2020)), which we assume to apply to the long-period comets. The resulting values of r_2 are also listed for each comet in Table 2.

The two estimates of the nucleus radii are compared in Figure 1. Ideally, we would find $r_1 = r_2$ (indicated in the Figure by the solid diagonal line) but the comets are better described by $r_1 \sim (5/3)r_2$ (shown as a dashed, black line in the figure). Sosa & Fernández (2011) found a similar result and interpreted it to mean that the long-period comets are hyperactive ($f_A > 1$ in Equation 5 acts to reduce r_1), allowing substantial sublimation from icy grains in the coma in addition to ice in the nucleus. However, the assumption of hyperactivity is only one of several possible reasons for the difference between r_1 and r_2 . Parameters k_R , and ρ_n in Equation 7 might also be different from the values assumed and radius estimate r_2 can be increased by increasing k_R and/or decreasing ρ_n . To consider one example, r_1 and r_2 could be brought into agreement if the bulk nucleus density in Equation 7 were arbitrarily reduced by a factor $(5/3)^3 \sim 5$ to $\rho_n \sim 100 \text{ kg m}^{-3}$ instead of 500 kg m^{-3} , as assumed. This lower density is by no means ruled out by physics and would

still be consistent with values measured in several short-period comets (e.g. 6P/d’Arrest, 19P/Borrelly) (Groussin et al. 2019). However, rather than make alternative, weakly justified guesses for some of the parameters in Equations 5 and 7, we conservatively choose the average radius, $\bar{r}_n = (r_1 + r_2)/2$, as our best estimate of the nucleus radius, and we take the difference between radii r_1 and r_2 as a crude measure of the intrinsic radius uncertainty. We feel that this is a good procedure because, if we instead followed Sosa & Fernández (2011) by assuming that $f_A > 1$, the conclusions to be reached (described in Section 4) would be changed only by becoming stronger. The mean radii are listed in column 4 of Table 3.

Figure 1 shows that the disintegrating long-period comets (filled red circles representing C/2001 A2, C/2010 X1, C/2012 S1, C/2017 E4, C/2019 Y4, C/2020 F8 and C/2021 A1) have smaller nuclei, on average, than those that survive perihelion (filled yellow circles). Six of the seven disintegrating comets are sub-kilometer bodies while the seventh (C/2001 A2 (LINEAR)) is only slightly larger at $\bar{r}_n = 1.4 \pm 0.4$ km (Table 2). The median radius of the disintegrating long-period nuclei is 0.41 km (mean value 0.55 ± 0.15 km, 7 objects) whereas that of surviving nuclei is 1.60 km (mean value 1.96 ± 0.28 km, 20 objects). The non-parametric KS test was used to assess the likelihood that the two radius distributions are drawn from the same population. This test gave a statistic $D = 0.807$, with an associated probability $p = 0.002$, consistent with the visual impression that the surviving and disrupted radius distributions are distinct. We also compared the distributions of perihelion distances of the surviving and disrupted comets. The median perihelion distance of the disrupted comets is 0.48 au (mean value 0.48 ± 0.09 au, 7 objects) while that of the survivors is 0.99 au (mean value 0.97 ± 0.10 au, 20 objects). The associated KS statistics are $D = 0.697$ and $p = 0.007$, indicating that the hypothesis that the two samples are drawn from the same parent population can again be rejected, although with less confidence.

Figure 2 compares the two measured quantities, the non-gravitational acceleration and the mass loss rate, both at 1 au. The figure shows that $\alpha_{NG}(1)$ and $\dot{M}(1)$ are inversely related, and with a trend that is readily understood. All else being equal, we expect that the mass loss rate should vary as $\dot{M}(1) \propto \bar{r}_n^{-2}$ (Equation 5), while the non-gravitational acceleration should vary as $\alpha_{NG}(1) \propto \dot{M}(1)/\bar{r}_n^3 \propto 1/\bar{r}_n$ (Equation 7), giving $\alpha_{NG}(1) \propto \dot{M}(1)^{-1/2}$. The black line in Figure 2 has slope -1/2 and evidently matches the data well. A least-squares fit of a power law (dashed red line in the figure) to the data gives $\alpha_{NG}(1) \propto \dot{M}(1)^B$ with $B = -0.66 \pm 0.17$, consistent with this expectation within one standard deviation. The color coding in Figure 2 also shows that comets with the largest non-gravitational accelerations and the weakest outgassing rates are the most likely to disintegrate, with an approximate separation between disintegrating and surviving comets at $\alpha_{NG}(1) \sim 10^{-6} \text{ m s}^{-2}$ and $\dot{M}(1) \sim 10^3 \text{ kg s}^{-1}$. By Equations 5 and 7, these values correspond to nucleus radii $r_n = 0.5$ to 0.9 km, consistent with the color-coding in Figure 1 showing that subkilometer long-period comet nuclei disintegrate.

Published examples of well-characterized sub-kilometer long-period comets are few and far between; the compilation by Lamy et al. (2004) lists only two. C/1999 S4 (LINEAR) had $r_n = 0.45$ km (Altenhoff et al. 2002), $q = 0.765$ au and disintegrated spectacularly at perihelion (Weaver et al. 2001), consistent with our findings here. C/1983 J1 (Sugano-Saigusa-Fujikawa) had $r_n < 0.37$ km (Hanner et al. 1987), $q = 0.47$ au but was observed only for a few weeks when near Earth so that its fate is unknown. The paucity of well-studied small nuclei relative to power-law extrapolations from larger sizes (Bauer et al. 2017) may itself be evidence for the efficient destruction of sub-kilometer long-period comet nuclei.

4. DISCUSSION

Seven of the 27 LPCs in our sample either fragmented or disintegrated, fates that are indicated in column 9 of Table 3 by the letters “F” and “D”, respectively. These descriptors are purely morphological; in fragmentation the comet splits into two or more discrete objects typically each retaining a cometary appearance, while in disintegration the comet assumes the appearance of an expanding, diffuse cloud, lacking an obvious source or other embedded structure. The physical relationship between fragmentation and disintegration is unclear. We assume that the former is a mild case of the latter and, for simplicity in the following discussion, we use the term “disintegration” to apply to both.

4.1. Disintegration Mechanisms

Given the results in Figures 1 and 2, what mechanisms could be responsible for the disintegration of long-period nuclei?

Tidal Breakup: The Roche radius of the Sun for a comet nucleus represented as a fluid body of density $\rho_n = 500 \text{ kg m}^{-3}$ is $\sim 10^{-2}$ au. In our sample, only C/2012 S1 (ISON) approached the Sun closely enough ($q = 0.012$ au) for tidal disruption to be possible. Neither have the remaining comets passed within the Roche spheres of any planet, eliminating tidal breakup as a generally relevant mechanism for this study.

Sublimation: Sublimation erosion is typically ~ 10 m per orbit (computed from Equation 3), and thus is too slow to destroy a ~ 1 km diameter nucleus in the ~ 1 year spent in strong sublimation while close to the Sun. Moreover, sublimation would naturally produce more steady erosion of the comet, not the catastrophic disintegrations as observed.

Collisional Disruption: Interplanetary collisions are very rare. Even in the relatively dense asteroid belt, the collisional disruption timescales of sub-kilometer bodies are

measured in 100s of Myr, such that the probability of a destructive collision in the ~ 1 year spent by each comet near the Sun is negligible. Moreover, the long-period comets have large orbits with random inclinations and disintegrate far above the ecliptic plane, where collisional disruption is even less likely.

Confined Pressure Explosion: Samarasinha (2001) invoked the build-up of gas pressure in order to explain cometary disruption. The problem with this mechanism is that the effect of heating by the Sun is confined to a thermal skin that is very thin compared to the radius of the nucleus. For example, cometary material has very small diffusivity, resulting in a thermal skin depth ($\sim 10^{-2}$ m) that is very small compared to the nucleus radius. Unless the full body of the nucleus is permeated by large interconnected voids (but still sealed from the vacuum of surrounding space), any gas pressure build-up must be confined to a thin surface shell incapable of disrupting of the whole nucleus. Likewise, crystallization runaways, although potentially capable of triggering cometary outbursts (Prialdnik & Bar-Nun 1992), are necessarily confined by the radial temperature gradient to a surface shell with thickness $\ll r_n$.

Rotational Instability: Outgassing exerts a torque on the cometary nucleus capable of substantially changing the spin on a timescale given by

$$\tau_s = \left(\frac{16\pi^2}{15} \right) \left(\frac{\rho_n r_n^4}{k_T V_{th} P} \right) \left(\frac{1}{\overline{M}} \right). \quad (9)$$

Here, P is the instantaneous spin-period, k_T is the dimensionless moment arm, equal to the fraction of the outflow momentum that exerts a torque on the nucleus and \overline{M} is the average value of the mass loss rate following the comet in its orbit (Jewitt 2021). For a weakly cohesive nucleus, the end-state of spin-up is rotational disruption into fragments which are themselves subject to rapid disintegration because of the strong dependence of τ_s on r_n (Equation 9) and because of the sudden exposure of previously buried volatiles.

To calculate \overline{M} , we use the facts that water is the dominant volatile and that strong sublimation of water ice is restricted to heliocentric distances $r_H \lesssim 3$ au. Species more volatile than water (notably CO, CO₂) can sublimate at lower temperatures and larger distances but their abundances are poorly constrained in our sample of comets and, in the interests of simplicity, we do not consider them here. Their inclusion would only strengthen our conclusions by amplifying the importance of outgassing torques relative to our water ice calculation. Accordingly, we computed the average mass loss rate for each comet using

$$\overline{M} = \frac{\int_{t_0}^{t_0+\Delta t} \dot{M}(r_H(t)) dt}{\Delta t} \quad (10)$$

where t_0 is the pre-perihelion time at which $r_H = 3$ au and Δt is the time spent with $r_H \leq 3$ au. The instantaneous mass loss rate $\dot{M}(r_H(t))$ is computed by solving Kepler’s law for $r_H(t)$ and using Equation 3 to find $\dot{M}(r_H(t)) = 2\pi f_s(r_H(t))\overline{r}_n^{-2}$. The average, listed in Table 3, is then substituted into Equation 9 in order to calculate the characteristic spin-up time, τ_s .

We again used values of the quantities k_T , ρ_n and P taken from the cometary literature. The median dimensionless moment arm, $k_T = 0.007$, is determined from measurements of the nuclei of short-period comets (Jewitt 2021). Likewise, the average nucleus density, $\rho_n = 480 \pm 220$ kg m⁻³, is known only for the nuclei of short-period comets (Groussin et al. 2019). We adopt $P = 15$ hours, equal to the median rotation period measured in short-period comets (Jewitt 2021). While there are no clear reasons to think that the median k_T , ρ_n and P should be different in the long-period vs. short-period comets, we are aware of this possibility and eagerly await direct measurements of these parameters in the former population. Given the uncertainties in these quantities, it is obvious that Equation 9 can provide, at best, a value of τ_s accurate to no better than order of magnitude.

We set a simple criterion for judging the importance of spin-up torques by comparing

τ_s with Δt , defined above as the time spent by each comet with $r_H \leq 3$ au. If $\tau_s < \Delta t$ then sublimation torques can substantially modify the nucleus spin within a single perihelion passage of the comet, potentially leading to rotational instability and breakup. Otherwise, the outgassing torques are too weak to trigger rotational breakup, at least within a single perihelion passage. Values of Δt and τ_s are listed in Table 3 and plotted for convenience in Figure 3. The table and figure show that six of the seven disintegrated comets in our sample had $\tau_s < \Delta t$, consistent with rotational breakup as the cause of their destruction. The seventh (C/2001 A2) also satisfies this inequality within the error bar on τ_s . Those comets which did not breakup or disintegrate have $\tau_s > \Delta t$, again with some ambiguous cases close to the $\tau_s = \Delta t$ line. Again, while emphasizing the (necessarily) order of magnitude nature of the treatment offered in Section 3.1 the basic result, that the disintegrating nuclei are those with the shortest spin-up times, is remarkable.

Figure 4 shows the mass loss rate at $r_H = 1$ au vs. the nucleus radius, \bar{r}_n . The solid black line in the figure shows $\dot{M}(1) = 1850\bar{r}_n^2$, with \bar{r}_n in km and $\dot{M}(1)$ in kg s^{-1} . Substituting for $\dot{M}(1)$ in Equation 9 and setting $\tau_s = \Delta t = 1$ year, we calculate the critical radius below which the average long-period comet is susceptible to rotational break-up in a single perihelion passage as $r_n \sim 1$ km, in agreement with the observation that the disintegrating long-period comets are sub-kilometer objects.

4.2. Relation to the Oort Fading Parameter

Long-period comets with reciprocal semimajor axes $a^{-1} < 10^{-4}$ au $^{-1}$ are known as “Oort spike” comets, some but not all of which are dynamically new objects making their first pass through the planetary region. Oort (1950) found that a purely dynamical model of comet delivery from a distant reservoir predicts a larger flux of returning objects, relative to dynamically new comets, than is observed. He introduced an ad hoc “fading parameter”

to bring the dynamical model into agreement with the data. The need for this fading parameter has since been confirmed many times (e.g. Wiegert & Tremaine (1999); Levison et al. (2002); Neslušan (2006)) but the physical cause of the fading remains unknown. Oort (1950) and others conjecture that it is due to “surface aging” in response to insolation. Levison et al. (2002) concluded from the small number of detections of returning objects in ground-based surveys that a majority of dynamically new comets are destroyed, not merely faded.

The present work shows that disintegration, by removing comets from the observable sample, is a significant fading mechanism. The destruction is size dependent, preferentially afflicting small nuclei, and also perihelion distance dependent, being more probable at small distances than at large. In contrast, published models of the fading parameter instead assume a survival probability that is independent of nucleus size (Wiegert & Tremaine (1999); Levison et al. (2002)). Wiegert & Tremaine (1999) examined a sample of comets having median perihelion $q \sim 1$ au, comparable to that of our sample in Table 1. As one of several possible solutions, they found a fading law in which the comets are divided into two groups and supposed that some 95% of long-period comets are destroyed within the first six perihelion passages while the remaining 5% survive indefinitely. We conjecture that this empirical division into two groups is an artifact of size-dependent rotational disruption; 95% of the long-period comets are sub-kilometer objects subject to rotational disruption in a few orbits while 5% are larger and can resist disruption for a much longer time.

The implication that only 5% of long-period comet nuclei have $r_n > 1$ km at first appears at odds with the radius distribution of the nuclei listed in Table 3, where 17 of the 27 nuclei (62%) are larger than 1 km. However, our sample is highly observationally biased against the inclusion of small nuclei because they produce too little H₂O to be detected in the flux-limited Lyman- α data from SWAN. (The largest comets are also excluded because

their non-gravitational accelerations are too small to be measured). As a result, the data in Table 3 severely underestimate the abundance of small LPC nuclei, and cannot be used to assess the intrinsic size distribution of the nuclei.

Cometary fading has been reported to extend to at least $r_H \sim 10$ au (Królikowska & Dybczyński 2019; Kaib 2022), far beyond the region where outgassing torques from sublimating water ice can alter the nucleus spin. Moreover, a growing number of observations show activity in distant comets (e.g. $\sim 20 - 25$ au in the case of C/2014 UN271 Bernardinelli-Bernstein (Farnham et al. 2021) and even 35 au in the case of C/2017 K2 (PANSTARRS) (Jewitt et al. 2021)). Fragmentation has also been inferred at very large distances, for example in comets C/2002 A1 and A2, reported to have split from a common parent when inbound at $r_H \sim 22.5$ au (Sekanina et al. 2003). Water ice is involatile beyond 5 or 6 au and the sublimation of a more volatile material, perhaps carbon monoxide (CO) ice, is a leading candidate for driving this distant cometary activity. Could fading at large distances be due to torques from CO sublimation?

A definitive answer to this question cannot be reached given our limited knowledge of the surface properties of distant comets, or calculated from first principles. However, order of magnitude scaling considerations strongly suggest an answer in the negative, as follows. To first order, the ratio of the timescale for spin-up of a given body through sublimation of CO to that for spin-up through sublimation of water ice is (c.f. Equation 9)

$$\frac{\tau_s(\text{CO})}{\tau_s(\text{H}_2\text{O})} \sim \frac{\dot{M}(\text{H}_2\text{O}) V_{th}(\text{H}_2\text{O})}{\dot{M}(\text{CO}) V_{th}(\text{CO})}. \quad (11)$$

We compare the sublimation of CO at 10 au to that of H₂O at 1 au. Fortunately, measurements of the two ratios on the right hand side of Equation 11 are available for the long-period comet C/1995 O1 (Hale-Bopp). There, $\dot{M}(\text{H}_2\text{O}, r_H = 1 \text{ au})/\dot{M}(\text{CO}, r_H = 10 \text{ au}) \sim 10^3$ (Figure 5 of Biver et al. (2002)) and $V_{th}(\text{H}_2\text{O}, r_H = 1 \text{ au})/V_{th}(\text{CO}, r_H =$

10 au) ~ 3 (figure 4a of Biver et al. (2002)), giving $\tau_s(\text{CO}, r_H = 10 \text{ au})/\tau_s(\text{H}_2\text{O}, r_H = 1 \text{ au}) \sim 3000$. This factor of 3000 is partly compensated by the longer time spent in the CO sublimation zone. C/1995 O1 had $r_H < 30$ au for 27 years (compared with $\Delta t \sim 1$ year for the comets in Table 1) and could have sublimated CO the entire time. Still, based on this scaling argument, spin-up timescales for a given object at 10 au remain two orders of magnitude larger than at 1 au, given C/Hale-Bopp-like outgassing behavior. Substantial spin-up due to CO torques seems unlikely unless the CO/H₂O ratios in other LPCs are much larger than measured in C/1995 O1. On this basis we conclude that, while important in the water sublimation zone, spin-up destruction is not an obvious cause of spin-up or fading in any but the tiniest comets beyond it. Oort’s fading parameter thus seems likely to have several physical origins of which rotational disruption is only one.

For LPCs with $q \lesssim 3$ au, we offer three predictions that will be observationally testable in the foreseeable future given improved population data. First, LPC nuclei larger than a few km in radius should rarely disrupt or disintegrate, unless by another process (e.g. tidal disruption, as may be the case for C/2012 S1 (ISON)). Second, the size distribution of LPCs should be flattened at radii $r_n \lesssim 1$ km, relative to its value at larger radii, owing to the selective loss of small nuclei through rotational instability. Third, accurately bias-corrected data should show that the size distributions of long-period comet nuclei vary with q , reaching “primordial” values only in the outer solar system where mass loss is negligible.

Lastly, it is reasonable to expect that the imprints of rotational disruption might be found in the Damocloid population, to the extent that these objects (inactive bodies with Tisserand parameters $T_J \leq 2$) are remnants of formerly active long-period comets. Measurements indeed show a flatter size distribution (Kim et al. 2014), consistent with the preferential destruction of smaller Damocloids, but the available sample is small and undoubtedly subject to its own biases. Future work on these objects may also be revealing.

5. SUMMARY

We examine a sample of 27 long-period comets for which both non-gravitational accelerations and water production rates are available. Using these two measured quantities we are able to estimate the nucleus sizes, and so to explore the systematics of this population. Seven of the 27 comets ($\sim 25\%$) fragmented or disintegrated.

- The disintegrating cometary nuclei have systematically smaller radii (median 0.4 km, 7 objects) than those that survive in proximity to the Sun (1.6 km, 20 objects).
- The disintegrating comets have smaller perihelion distance (median 0.5 au, 7 objects) than those surviving (1.0 au, 20 objects).
- These size and perihelion distance trends are both consistent with nucleus disintegration through rotational instability, triggered by outgassing torques from sublimating water ice. Specifically, the timescale for outgassing torques to change the spin of sub-kilometer nuclei is less than the time spent in strong sublimation.
- Rotational disruption is a cause of the “fading” required to fit the orbital semimajor axis distribution of long-period comets.

I thank the anonymous referee for highlighting the importance of fading at large distances, Yoonyoung Kim for additional comments on the manuscript and Man-To Hui for advice about the vagaries of JPL Horizons. Based in part on observations made under GO 16929 with the NASA/ESA Hubble Space Telescope, obtained at the Space Telescope Science Institute, operated by the Association of Universities for Research in Astronomy, Inc., under NASA contract NAS 5-26555.

REFERENCES

- A'Hearn, M. F., Millis, R. C., Schleicher, D. O., et al. 1995, *Icarus*, 118, 223.
doi:10.1006/icar.1995.1190
- Altenhoff, W. J., Bertoldi, F., Menten, K. M., et al. 2002, *A&A*, 391, 353. doi:10.1051/0004-6361:20020783
- Bauer, J. M., Grav, T., Fernández, Y. R., et al. 2017, *AJ*, 154, 53. doi:10.3847/1538-3881/aa72df
- Bertaux, J. L., Quémerais, E., Lallement, R., et al. 1997, *Sol. Phys.*, 175, 737.
doi:10.1023/A:1004979605559
- Bortle, J. E. 1991, *International Comet Quarterly*, 13, 89
- Biver, N., Bockelée-Morvan, D., Colom, P., et al. 2002, *Earth Moon and Planets*, 90, 5.
doi:10.1023/A:1021599915018
- Combi, M. R., Mäkinen, J. T. T., Henry, N. J., et al. 2008, *AJ*, 135, 1533. doi:10.1088/0004-6256/135/4/1533
- Combi, M. R., Mäkinen, J. T. T., Bertaux, J.-L., et al. 2009, *AJ*, 137, 4734. doi:10.1088/0004-6256/137/6/4734
- Combi, M. R., Boyd, Z., Lee, Y., et al. 2011, *Icarus*, 216, 449.
doi:10.1016/j.icarus.2011.09.019
- Combi, M. R., Fougere, N., Mäkinen, J. T. T., et al. 2014, *ApJ*, 788, L7. doi:10.1088/2041-8205/788/1/L7
- Combi, M. R., Mäkinen, T. T., Bertaux, J.-L., et al. 2018, *Icarus*, 300, 33.
doi:10.1016/j.icarus.2017.08.035

Combi, M. R., Mäkinen, T. T., Bertaux, J.-L., et al. 2019, *Icarus*, 317, 610.

doi:10.1016/j.icarus.2018.08.031

Combi, M. R., Shou, Y., Mäkinen, T., et al. 2021, *Icarus*, 365, 114509.

doi:10.1016/j.icarus.2021.114509

Combi, M., Makinen, T., Bertaux, J.-L., et al. 2021, AAS Division of Planetary Science meeting 53, id. 210.02. *Bulletin of the American Astronomical Society*, Vol. 53, No. 7 e-id 2021n7i210p02

Faggi, S., Villanueva, G. L., Mumma, M. J., et al. 2018, *AJ*, 156, 68. doi:10.3847/1538-3881/aace01

Farnham, T. L., Kelley, M. S. P., & Bauer, J. M. 2021, *Plan. Sci. J.*, 2, 236.

doi:10.3847/PSJ/ac323d

Groussin, O., Attree, N., Brouet, Y., et al. 2019, *Space Sci. Rev.*, 215, 29. doi:10.1007/s11214-019-0594-x

Hanner, M. S., Newburn, R. L., Spinrad, H., et al. 1987, *AJ*, 94, 1081. doi:10.1086/114544

Jewitt, D. 2015, *AJ*, 150, 201. doi:10.1088/0004-6256/150/6/201

Jewitt, D., Kim, Y., Mutchler, M., et al. 2020, *ApJ*, 896, L39. doi:10.3847/2041-8213/ab99cb

Jewitt, D. 2021a, *AJ*, 161, 261. doi:10.3847/1538-3881/abf09c

Jewitt, D., Kim, Y., Mutchler, M., et al. 2021b, *AJ*, 161, 188. doi:10.3847/1538-3881/abe4cf

Kaib, N. A. 2022, *Science Advances*, 8, eabm9130. doi:10.1126/sciadv.abm9130

Kim, Y., Ishiguro, M., & Usui, F. 2014, *ApJ*, 789, 151. doi:10.1088/0004-637X/789/2/151

Królikowska, M. & Dybczyński, P. A. 2019, *MNRAS*, 484, 3463. doi:10.1093/mnras/stz025

- Lamy, P. L., Toth, I., Fernandez, Y. R., et al. 2004, in *Comets II*, M. C. Festou, H. U. Keller, and H. A. Weaver (eds.), University of Arizona Press, Tucson, 745 pp., p.223-264
- Levison, H. F., Morbidelli, A., Dones, L., et al. 2002, *Science*, 296, 2212.
doi:10.1126/science.1070226
- Marsden, B. G., Sekanina, Z., & Yeomans, D. K. 1973, *AJ*, 78, 211. doi:10.1086/111402
- Neslušan, L. 2006, *Contributions of the Astronomical Observatory Skalnaté Pleso*, 36, 5
- Oort, J. H. 1950, *Bull. Astron. Inst. Netherlands*, 11, 91
- Prialnik, D. & Bar-Nun, A. 1987, *ApJ*, 313, 893. doi:10.1086/165029
- Prialnik, D. & Bar-Nun, A. 1992, *A&A*, 258, L9
- Samarasinha, N. H. 2001, *Icarus*, 154, 540. doi:10.1006/icar.2001.6685
- Saki, M., Gibb, E. L., Bonev, B. P., et al. 2020, *AJ*, 160, 184. doi:10.3847/1538-3881/aba522
- Sekanina, Z., Chodas, P. W., Tichý, M., et al. 2003, *ApJ*, 591, L67. doi:10.1086/376977
- Sosa, A. & Fernández, J. A. 2011, *MNRAS*, 416, 767. doi:10.1111/j.1365-2966.2011.19111.x
- Weaver, H. A., Sekanina, Z., Toth, I., et al. 2001, *Science*, 292, 1329.
doi:10.1126/science.1058606
- Wiegert, P. & Tremaine, S. 1999, *Icarus*, 137, 84. doi:10.1006/icar.1998.6040

Table 1. Comet Sample

Comet	a^a	e^b	i^c	q^d	T_P^e	S/NS ^f
C/2000 WM1 (LINEAR)	1877	0.9997077	72.6	0.549	2452297.3	NS
C/2001 A2-A (LINEAR)	971	0.9991978	36.5	0.779	2452054.0	NS
C/2001 Q4 (NEAT)	16725	0.9999426	99.6	0.960	2453141.5	S
C/2002 T7 (LINEAR)	47471	0.9999870	160.6	0.615	2453118.5	S
C/2002 X5 (Kudo-Fujikawa)	1119	0.9998281	94.2	0.192	2452668.5	NS
C/2003 K4 (LINEAR)	29199	0.9999651	134.2	1.021	2453292.3	S
C/2004 Q2 (Machholz)	2528	0.9995221	38.6	1.208	2453395.5	NS
C/2009 P1 (Garradd)	2384	0.9993522	106.2	1.544	2455919.3	NS
C/2010 X1 (Elenin)	48388	0.9999900	1.8	0.482	2455815.2	S
C/2012 K1 (PANSTARRS)	26070	0.9999597	142.4	1.051	2456897.3	S
C/2012 S1 (ISON)	-144820	1.0000001	62.2	0.012	2456625.3	S
C/2012 X1 (LINEAR)	145	0.9889527	44.4	1.597	2456710.3	NS
C/2013 US10 (Catalina)	19030	0.9999569	148.9	0.820	2457342.3	S
C/2013 X1 (PANSTARRS)	3804	0.9996529	163.2	1.320	2457499.3	NS
C/2014 E2 (Jacques)	807	0.9991826	156.4	0.664	2456841.0	NS
C/2014 Q1 (PANSTARRS)	841	0.9996251	43.1	0.315	2457210.0	NS
C/2014 Q2 (Lovejoy)	502	0.9974320	80.3	1.290	2457052.5	NS
C/2015 ER61 (PANSTARRS)	718	0.9985315	6.3	1.054	2457883.5	NS
C/2015 G2 (MASTER)	6103	0.9998724	147.6	0.779	2457166.2	NS
C/2015 V2 (Johnson)	2525	0.9999546	49.9	1.631	2457916.8	NS
C/2017 E4 (Lovejoy)	821	0.9994044	88.2	0.489	2457866.8	NS
C/2017 T2 (PANSTARRS)	36830	0.9999560	57.2	1.619	2458974.5	S
C/2019 Y1 (ATLAS)	209	0.9959967	73.3	0.836	2458924.0	NS
C/2019 Y4-B (ATLAS)	501	0.9994983	45.4	0.251	2459000.5	NS
C/2020 F8 (SWAN)	-4886	1.0000874	110.8	0.427	2458997.0	S
C/2020 S3 (Erasmus)	191	0.9978918	19.9	0.403	2459196.3	NS
C/2021 A1 (Leonard)	2028	0.9996965	132.7	0.616	2459582.8	NS

^aBarycentric semimajor axis, in au

^bEccentricity

^cInclination, in degrees

^dPerihelion distance, in au

^eMean Julian Date of Perihelion

^fS = Spike, NS = Non-Spike

Table 2. Measured Properties

Comet	A_1^a	A_2^a	A_3^a	α_{NG}^b	$Q_{H_2O}(1)^c$	Source ^d
C/2000 WM1 (LINEAR)	5.8e-09	-8.0e-11	0	1.2e-07	1.7e+29	C19
C/2001 A2 (LINEAR)	-2.1e-08	1.9e-08	0	5.7e-07	1.4e+29	C08
C/2001 Q4 (NEAT)	1.6e-08	4.8e-10	4.3e-10	3.2e-07	5.3e+29	C09
C/2002 T7 (LINEAR)	1.2e-08	9.6e-10	-1.8e-09	2.4e-07	7.3e+29	C19, S20
C/2002 X5 (Kudo-Fujikawa)	2.6e-08	5.8e-09	0	5.4e-07	7.5e+28	C11
C/2003 K4 (LINEAR)	8.1e-09	-3.6e-09	-5.6e-10	1.8e-07	5.2e+29	C19
C/2004 Q2 (Machholz)	1.2e-08	-1.1e-09	-2.3e-09	2.5e-07	6.2e+29	C19
C/2009 P1 (Garradd)	2.0e-08	-1.0e-09	0	4.0e-07	4.8e+29	C19
C/2010 X1 (Elenin)	-4.8e-08	6.3e-08	0	1.6e-06	7.4e+27	S11
C/2012 K1 (PANSTARRS)	2.2e-08	-1.6e-09	-2.6e-09	4.5e-07	2.0e+29	C19
C/2012 S1 (ISON)	8.5e-08	5.8e-09	0	1.7e-06	2.0e+28	C19
C/2012 X1 (LINEAR)	3.6e-08	2.2e-09	5.3e-09	7.3e-07	1.4e+29	L14
C/2013 US10 (Catalina)	7.6e-09	6.2e-11	1.6e-10	1.5e-07	2.2e+29	C19
C/2013 X1 (PANSTARRS)	2.0e-08	-4.1e-09	-7.3e-09	4.4e-07	5.7e+29	C19
C/2014 E2 (Jacques)	2.1e-08	-2.8e-09	0	4.3e-07	1.3e+29	C19
C/2014 Q1 (PANSTARRS)	7.9e-09	2.8e-09	-5.5e-09	2.0e-07	3.0e+28	C19
C/2014 Q2 (Lovejoy)	1.3e-09	-1.5e-09	-2.4e-09	6.3e-08	2.1e+30	C19
C/2015 ER61 (PANSTARRS)	5.6e-09	-3.5e-09	-4.6e-10	1.3e-07	8.6e+28	S20
C/2015 G2 (MASTER)	1.2e-08	5.9e-09	-4.3e-09	2.8e-07	5.4e+28	C19
C/2015 V2 (Johnson)	2.3e-08	-4.2e-09	-4.4e-09	4.8e-07	1.6e+29	C21
C/2017 E4 (Lovejoy)	1.8e-07	-7.6e-08	0	3.9e-06	1.4e+28	F18
C/2017 T2 (PANSTARRS)	3.6e-08	-7.1e-10	-3.2e-10	7.2e-07	3.1e+28	C21
C/2019 Y1 (ATLAS)	1.1e-08	0	0	2.2e-07	1.4e+28	C21
C/2019 Y4 (ATLAS)	2.9e-07	-9.1e-09	0	5.8e-06	1.0e+28	C21
C/2020 F8 (SWAN)	1.5e-07	-2.6e-08	0	3.1e-06	5.5e+27	C21
C/2020 S3 (Erasmus)	1.7e-08	6.3e-09	0	3.6e-07	6.0e+28	C21b
C/2021 A1 (Leonard)	5.8e-08	-2.0e-08	1.1e-08	1.3e-06	3.0e+28	C22

^aOrthogonal components of the non-gravitational acceleration (units au day⁻²) from JPL Horizons

^bTotal non-gravitational acceleration at $r_H = 1$ au (units m s⁻²) from Equation 1

^cWater production rate at $r_H = 1$ au, molecules s⁻¹

^dC08 = Combi et al. (2008), C09 = Combi et al. (2009), C11 = Combi et al. (2011), C19 = Combi et al. (2019), C21 = Combi et al. (2021), C21b = Combi et al. (2021b), C22 = M. Combi (private communication), F18 = Faggi et al. (2018), S11 = D. Schleicher (private communication, cited in ?), S20 = Saki et al. (2020)

Table 3. Derived Properties

Comet	r_1^a	r_2^b	\bar{r}^c	$Q_{H_2O}^d$	\bar{M}^e	τ_s^f	Δt^g	Note ^h
C/2000 WM1 (LINEAR)	2.0	1.7	1.9	1.2e+29	3628	3.13	0.96	
C/2001 A2-A (LINEAR)	1.8	1.0	1.4	7.3e+28	2188	1.58	1.02	F
C/2001 Q4 (NEAT)	3.6	1.8	2.7	2.2e+29	6691	7.15	1.05	
C/2002 T7 (LINEAR)	4.2	2.2	3.2	4.7e+29	14263	6.65	0.98	
C/2002 X5 (Kudo-Fujikawa)	1.3	0.8	1.1	1.2e+29	3607	0.32	0.85	
C/2003 K4 (LINEAR)	3.5	2.2	2.8	2.1e+29	6252	9.79	1.07	
C/2004 Q2 (Machholz)	3.9	2.1	3.0	2.3e+29	6895	10.32	1.09	
C/2009 P1 (Garradd)	3.4	1.6	2.5	1.2e+29	3607	10.04	1.10	
C/2010 X1 (Elenin)	0.4	0.3	0.3	6.0e+27	180	0.07	0.94	D
C/2012 K1 (PANSTARRS)	2.2	1.2	1.7	8.8e+28	2645	2.79	1.07	
C/2012 S1 (ISON)	0.7	0.3	0.5	1.1e+29	3306	0.02	0.78	D
C/2012 X1 (LINEAR)	1.8	0.9	1.4	3.4e+28	1010	3.05	1.10	
C/2013 US10 (Catalina)	2.3	1.7	2.0	1.1e+29	3240	4.67	1.02	
C/2013 X1 (PANSTARRS)	3.7	1.7	2.7	1.7e+29	5140	9.31	1.09	
C/2014 E2 (Jacques)	1.8	1.0	1.4	8.3e+28	2501.0	1.38	0.99	
C/2014 Q1 (PANSTARRS)	0.8	0.8	0.8	3.4e+28	1010	0.43	0.89	
C/2014 Q2 (Lovejoy)	7.1	4.9	6.0	6.5e+29	19569	61.01	1.10	
C/2015 ER61 (PANSTARRS)	1.4	1.3	1.4	3.4e+28	1008	3.24	1.07	
C/2015 G2 (MASTER)	1.1	0.9	1.0	3.2e+28	973	0.99	1.02	
C/2015 V2 (Johnson)	2.0	1.1	1.5	3.8e+28	1154	4.18	1.10	
C/2017 E4 (Lovejoy)	0.6	0.2	0.4	1.1e+28	328	0.08	0.95	D
C/2017 T2 (PANSTARRS)	0.9	0.5	0.7	7.4e+27	223	0.98	1.09	
C/2019 Y1 (ATLAS)	0.6	0.6	0.6	6.7e+27	202	0.57	1.03	
C/2019 Y4 (ATLAS)	0.5	0.2	0.3	1.3e+28	393	0.03	0.87	F
C/2020 F8 (SWAN)	0.4	0.2	0.3	4.8e+27	143	0.04	0.92	D
C/2020 S3 (Erasmus)	1.2	0.8	1.0	5.6e+28	1677	0.60	0.92	
C/2021 A1 (Leonard)	0.8	0.4	0.6	1.9e+28	577	0.27	0.98	D

^aNucleus radius from Equation 5, km

^bNucleus radius from Equation 7, km

^cMean nucleus radius, km

^dAverage water production rate when $r_H \leq 3$ au

^eAverage mass production rate when $r_H \leq 3$ au, kg s^{-1}

^fSpin change timescale, from Equation 9, in years

^gElapsed time with $r_H \leq 3$ au, in years

^hD = Disintegrated, F = Fragmented

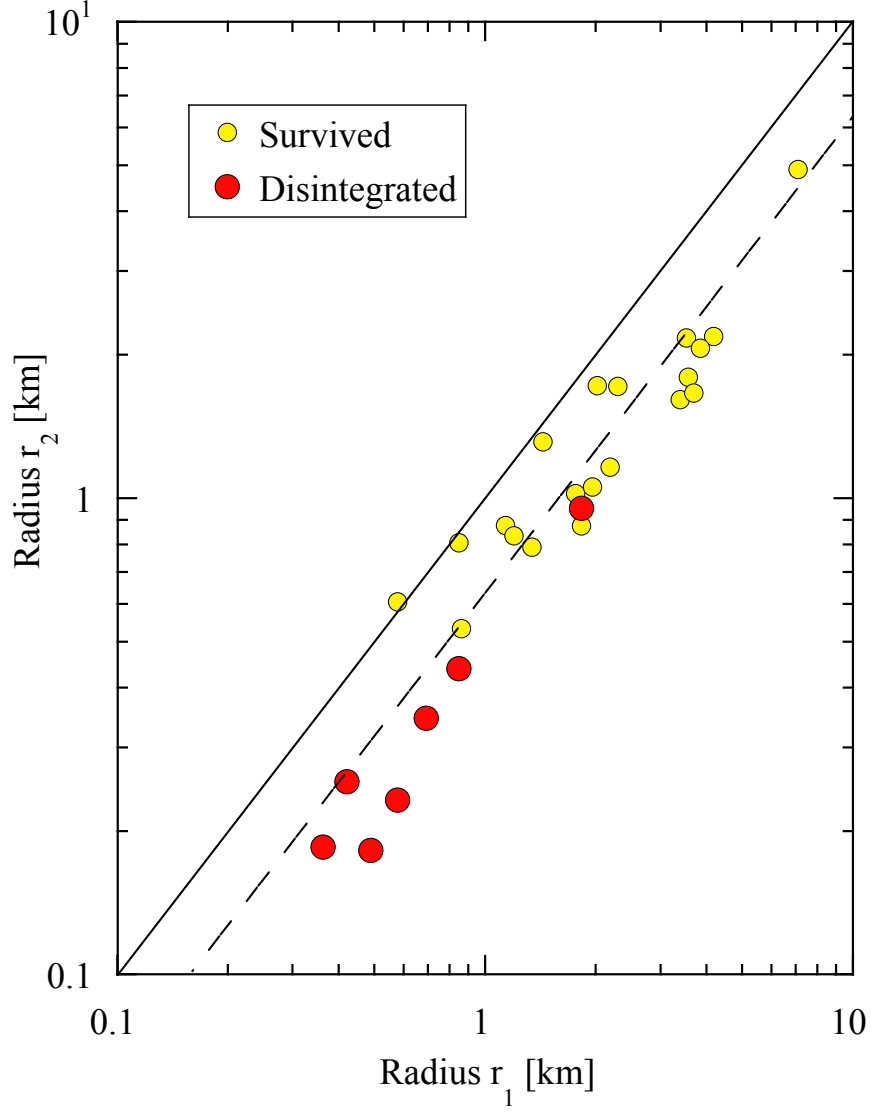


Fig. 1.— Nucleus radii independently estimated from the production rate (r_1 , from Equation 5) and the non-gravitational acceleration (r_2 , from Equation 7). Yellow and red-filled circles denote nuclei that survived and which were destroyed by the perihelion passage, respectively. The solid line shows $r_1 = r_2$. The dashed line indicates $r_1 = (5/3)r_2$.

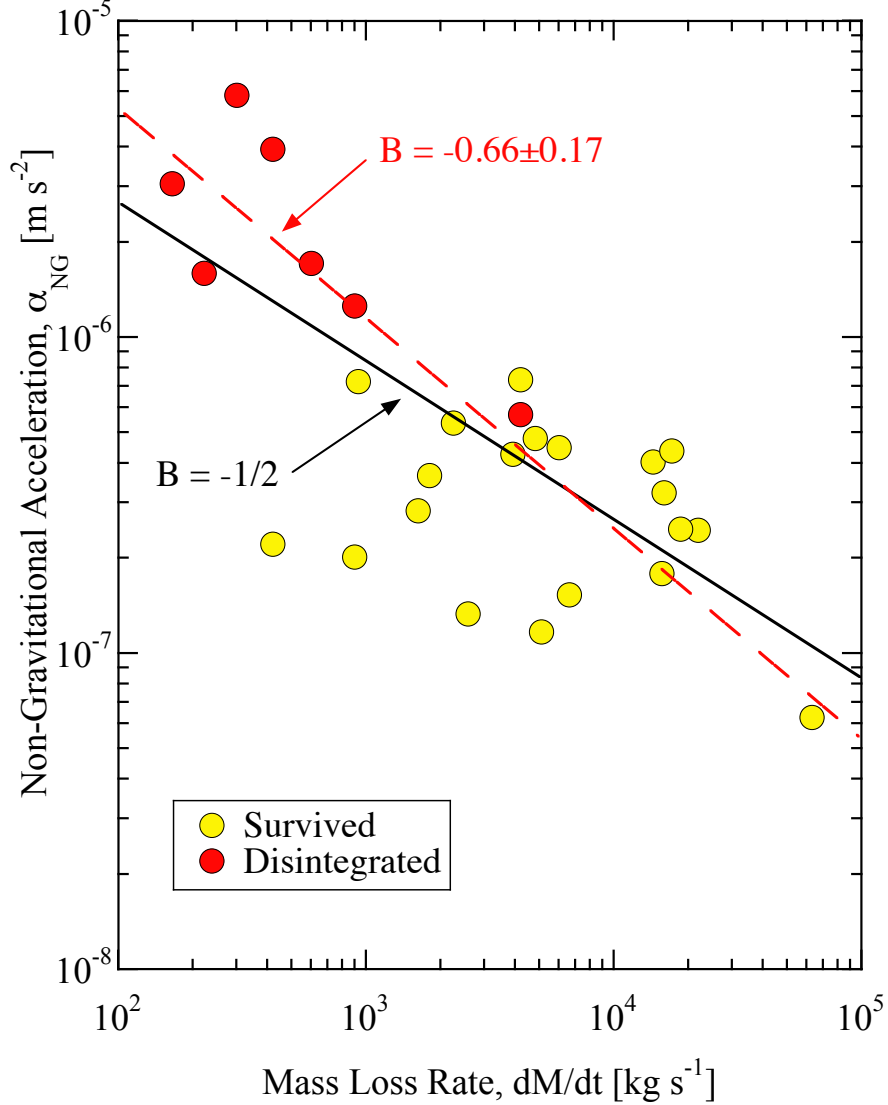


Fig. 2.— Non-gravitational acceleration, α_{NG} , as a function of the mass loss rate, \dot{M} , both referred to $r_H = 1$ au, computed from the data in Table 2. Yellow and red-filled circles denote nuclei that survived and which were destroyed by the perihelion passage, respectively. The solid black line has power-law slope $B = 0.5$. The red dashed line shows the least-squares fit and its index.

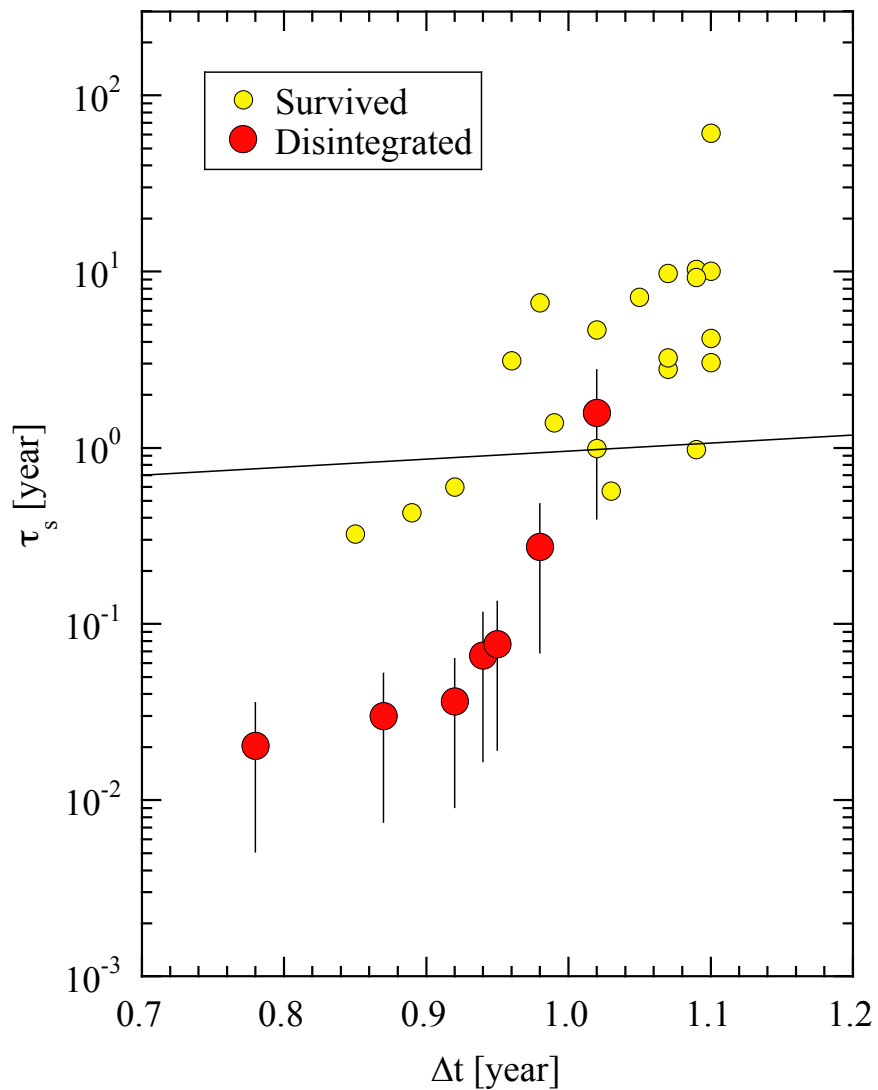


Fig. 3.— Sublimation timescale, τ_s (Equation 9) as a function of the time spent with $r_H < 3$ au. Yellow and red-filled circles denote nuclei that survived and which were destroyed by the perihelion passage, respectively. The solid black line marks $\tau_s = \Delta t$.

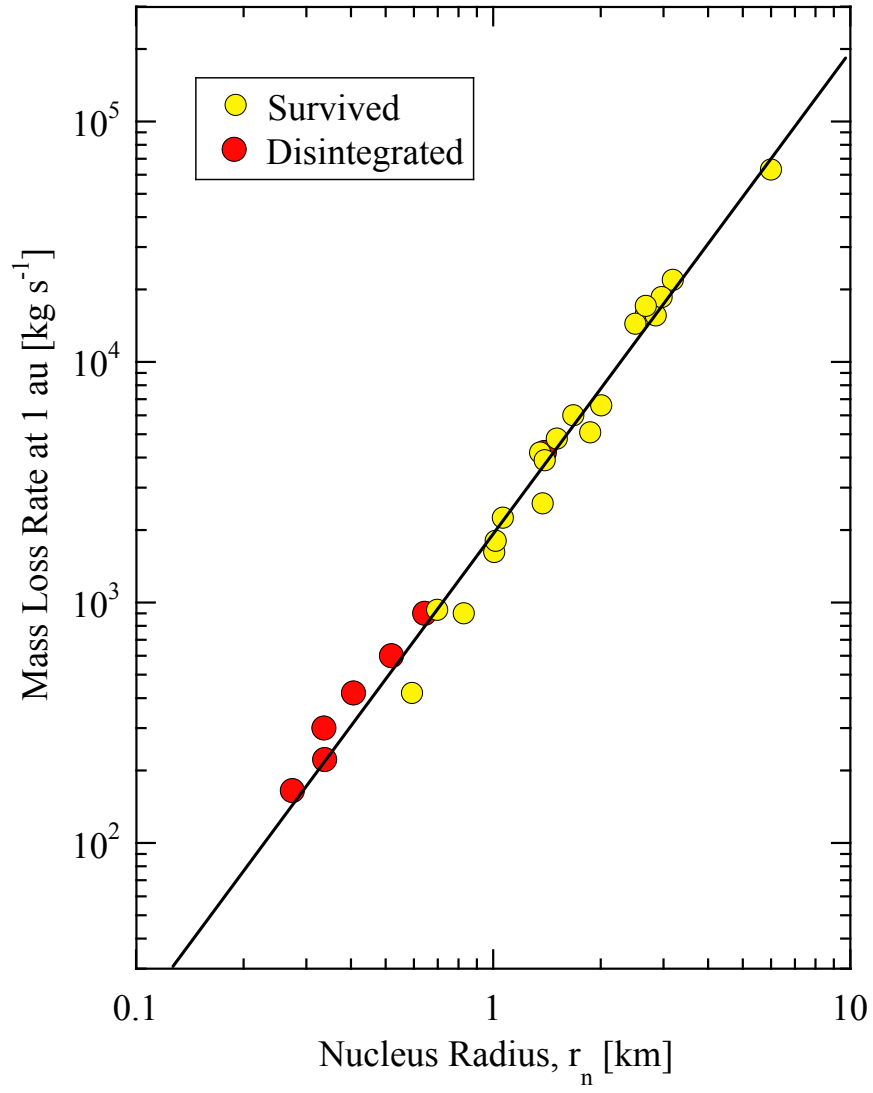


Fig. 4.— Mass loss rate vs. nucleus radius. The solid black line shows $\dot{M}(1) = 1850 r_n^{-2}$.